



Characteristics and dimensions of the infraorbital canal: a radiographic analysis using cone beam computed tomography (CBCT)

Marta Fontolliet¹ · Michael M. Bornstein² · Thomas von Arx³

Received: 10 January 2018 / Accepted: 28 September 2018 / Published online: 17 October 2018
© Springer-Verlag France SAS, part of Springer Nature 2018

Abstract

Purpose To analyze morphological characteristics and dimensions of the infraorbital canal-groove complex using cone beam computed tomography (CBCT), and to evaluate its relationship with adjacent anatomical structures.

Methods This retrospective study included CBCT scans of 100 patients taken between January and May 2014. Linear measurements of the infraorbital canal (IOC), the infraorbital groove (IOG) and the infraorbital canal-groove complex (IOC/G) were performed. Morphological variants of the IOC related to the maxillary sinus were classified into three types depending on the extent of protrusion of the canal into the sinus. Angles between the IOC and specific landmarks were measured to determine the direction of the IOC relative to the axial (A-ant) and sagittal (A-horiz) planes.

Results A total of 127 IOCs were analyzed. The mean length of the IOC/G was 29 ± 3.0 mm. This value comprised the mean distances of the IOC (24.4 ± 2.9 mm) and the IOG (4.6 ± 1.7 mm). For the different types of IOC morphology, Type 1 (IOC embedded in maxillary sinus roof) was the most common ($n = 87$, 68.5%). The mean angles of A-ant and A-horiz measured $48.9^\circ \pm 7.5^\circ$ and $20.3^\circ \pm 7.9^\circ$, respectively.

Conclusion Knowledge of the IOC/G morphology and its variants is important for the prevention of infraorbital nerve injury due to anesthesia or surgical interventions in this area. The presented data of anatomical characteristics of the IOC/G could be helpful for the planning of surgeries in the maxillary region by means of CBCT imaging.

Keywords Infraorbital canal · Infraorbital groove · Infraorbital canal-groove complex · Maxillary bone · Cone beam computed tomography

Introduction

The infraorbital canal (IOC) is located in the orbital floor. It terminates at the infraorbital foramen (IOF) below the orbital rim. The posterior part of the IOC is the infraorbital groove (IOG), which originates from the inferior orbital fissure (Fig. 1). The term infraorbital canal-groove complex (IOC/G) was first described by Scarfe et al. (1998) distinguishing three distinct structures: canal only, groove only and combination of groove and canal [13, 14].

The infraorbital nerve (ION) and infraorbital vessels run through the IOC, and their terminal branches exit via the IOF [5]. The ION is a branch of the maxillary nerve, which represents one of the three major trigeminal divisions [18]. The ION provides sensory innervation to the skin of the upper cheek, the lateral part of the nose, the skin and conjunctiva of the inferior eyelid, the skin and mucosa of the

✉ Thomas von Arx
thomas.vonarx@zmk.unibe.ch

Marta Fontolliet
marta.fontolliet@zmk.unibe.ch

Michael M. Bornstein
bornst@hku.hk

¹ Department of Reconstructive Dentistry and Gerodontology, School of Dental Medicine, University of Bern, Bern, Switzerland

² Oral and Maxillofacial Radiology, Applied Oral Sciences, Faculty of Dentistry, The University of Hong Kong, Hong Kong SAR, China

³ Department of Oral Surgery and Stomatology, School of Dental Medicine, University of Bern, Freiburgstrasse 7, 3010 Bern, Switzerland

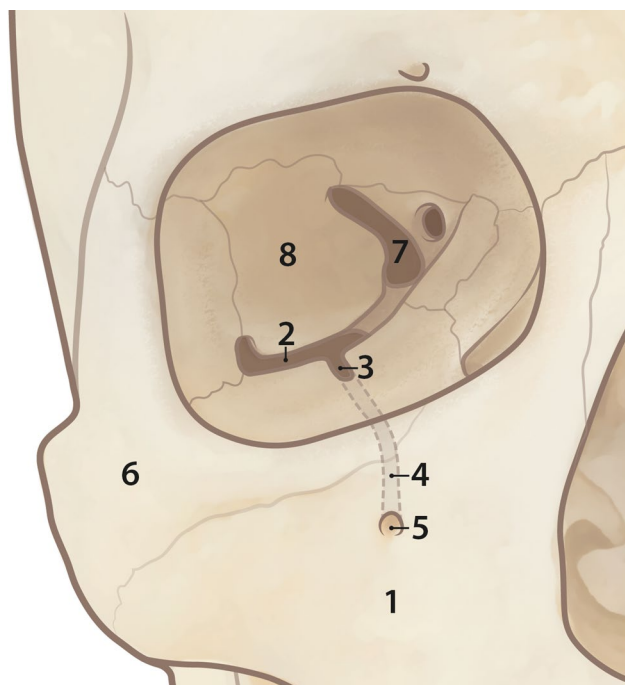


Fig. 1 The infraorbital canal-groove complex (IOC/G) is located in the maxillary bone (1). Originating from the inferior orbital fissure (2), the infraorbital groove (IOG) (3) is the posterior part of the IOC/G. It is followed by the infraorbital canal (IOC) (4), which is covered by the orbital floor and terminates at the infraorbital foramen (IOF) (5). Adjacent anatomical structures include the zygomatic bone (6), the superior orbital fissure (7), and the greater wing of the sphenoid bone (8)

upper lip, the mucosa of the maxillary sinus, the maxillary incisor, canine and premolar teeth and adjacent gingiva [9].

The ION requires anesthesia for interventions in dentistry, maxillofacial surgery, oto-rhino-laryngology and ophthalmology [9, 17]. To apply an infraorbital nerve block, to perform surgeries and to avoid intraoperative complications, the surgeon must be aware of the location of the IOF as well as of the morphology and course of the IOC/G. Different studies have described the morphology and the anatomical relations of the IOC/G using human skulls, cephalometric analysis or three-dimensional models based on CT scans [1, 4–6, 9, 12–15, 19]. However, there is only limited data available in the literature with regard to the anatomy of the IOC/G using cone beam computed tomography (CBCT) [12].

The aim of this study was to analyze the morphological characteristics of the IOC/G using CBCT imaging and to compare the results with available clinical and radiographic data in the literature. The primary objective of this study was to measure the dimensions of the IOC/G in CBCT images. Secondary aims included the morphological variants and the course of the IOC/G as well as its relationship to adjacent anatomical structures.

Materials and methods

Study design and population

This retrospective study included patients who had undergone CBCT scanning from January to May 2014 at the Department of Oral Surgery and Stomatology, University of Bern, Switzerland. The analysis was approved by the ethical committee of the State of Bern (approval number KEK-BE 252/2015). The study was conducted in full accordance with the Declaration of Helsinki 2013 (<http://www.wma.net>). The primary outcomes included the length and diameter of the IOC/G. The secondary outcomes were focused on age and gender of the patients, the angle between the IOC and specific landmarks, the IOC type, the frequency of maxillary sinus septa in relation to the IOC, and the branching location of the canalis sinuosus from the IOC.

Radiographic image analysis

CBCT scans (3D Accuitomo 170; Morita, Kyoto, Japan) were taken with voxel sizes ranging from 0.125 to 0.25 mm and exposure settings of 5.0–7.0 mA/80 kV. The cylindrical CBCT volumes (fields of view) measured 60 × 60 mm, 80 × 80 mm, 100 × 100 mm or 140 × 100 mm. All images were examined using a dedicated software (i-Dixel, Morita, Kyoto, Japan).

Inclusion criteria of CBCT scans were: patients had to be older than 18 years; the whole course of the IOC and the orbital floor were visible either on one side or bilaterally. Scans with traumatic, neoplastic or inflammatory lesions that might influence the anatomy of the IOC were excluded. The analysis was performed by one calibrated observer (MF). To assess intraobserver agreement, second measurements of a randomly (<http://www.random.org>) selected group of 20 patients with a total of 22 sites were performed after an interval of at least two months.

To obtain a reproducible position of the IOC, the images were adjusted according to specific landmarks (e.g., nasal septum, nasal floor) before measurement taking. The sagittal plane was positioned by moving the plane from the anterior nasal spine/nasal septum to a level at which the whole course of the IOC could be determined. The coronal plane was chosen at the level where the IOC was protruding the most into the maxillary sinus. The axial plane was positioned parallel to the nasal floor/hard palate and passed through the IOC.

The measurements of the IOC/G dimensions were performed using sagittal CBCT views (Fig. 2). The length of the IOC/G was determined using the methodology described by Przygocka et al. [13]:

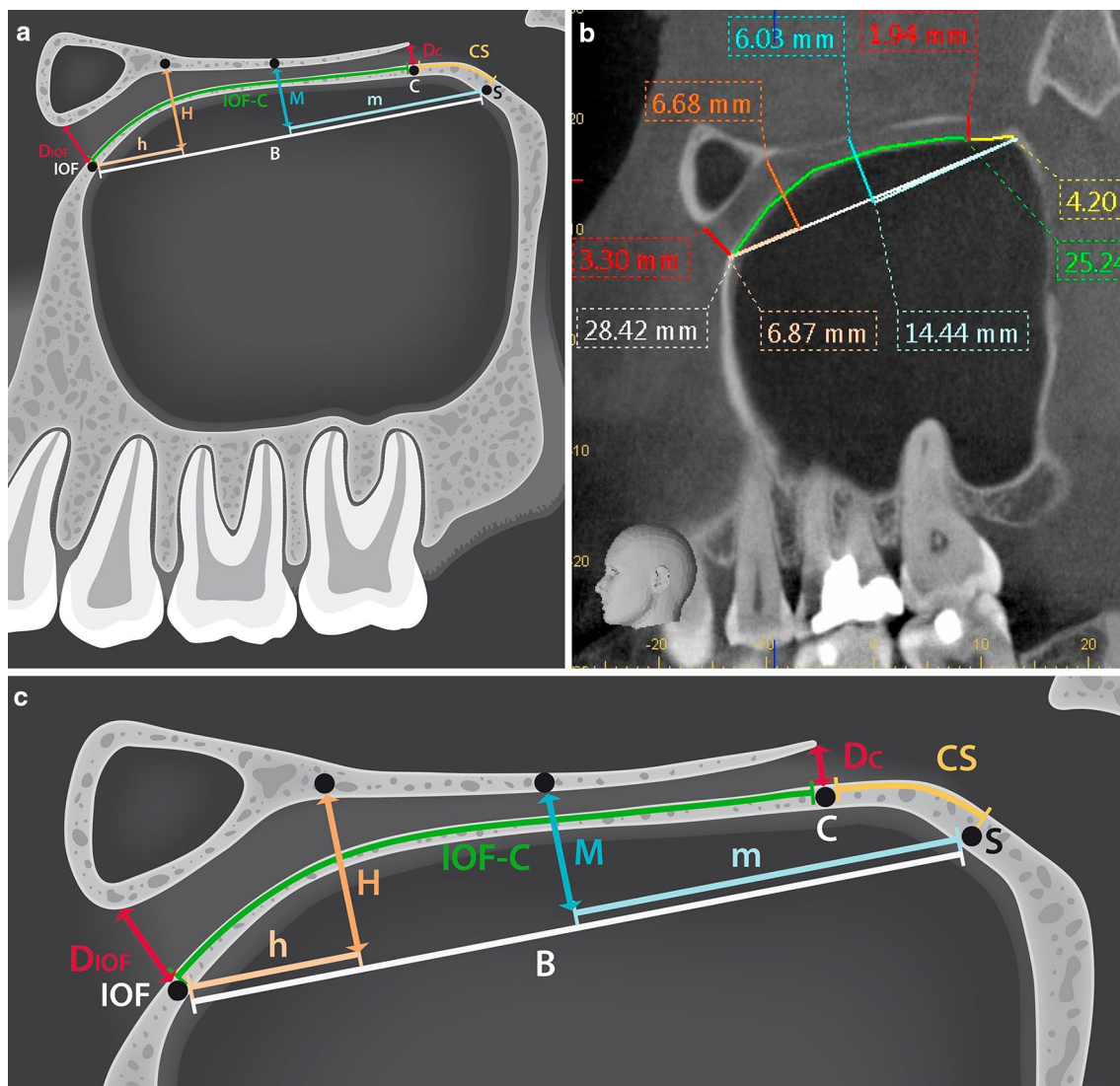


Fig. 2 Linear measurements of the IOC/G (IOF-C-S) were taken in sagittal CBCT planes: schematic overview of the measurements taken (a), representative sagittal scan of the linear measurements taken using the dedicated software (b), detailed schematic view of the linear measurements (c). The length of the infraorbital canal (IOF-C, green), the length of the infraorbital groove (C-S, yellow), the diameter of the IOC at the IOF (D_{IOF} , red) and at the posterior margin of

the IOC (D_C , red), the direct distance between IOF and S (B, white), and the distance at the midpoint of B (m, light blue) were measured. The perpendicular distances from the canal roof to B at its midpoint (M, blue), and the point where the perpendicular distance to B (H, orange) was highest, were also analyzed. Furthermore, the distance from line H to IOF (h, light orange) was measured. (Colour figure online)

- *IOF-C (IOC)* The distance (mm) between the lower-anterior margin of the infraorbital foramen (IOF) and the posterior margin of the IOC (C) covered by the bone of the orbital floor on a segmented curve (green line).
- *C-S (IOG)* The distance (mm) between the anterior (C) and the posterior (S) margins of the IOG on a segmented curve (yellow line). The position of the posterior margin (S) was defined as the site of the IOC opposite the orbital face of the greater wing of the sphenoid bone.
- *IOF-C-S (IOC/G)* The total length (mm) of the IOC/G was defined as the IOF-C plus C-S distance on a segmented curve.
- *Line B* The direct distance between the IOF and S (white line, straight).

The diameter of the IOC was measured perpendicularly at the IOF (D_{IOF}) and at the posterior margin (D_C) of the IOC (C) (red lines). Additional distances were measured as follows (Fig. 2):

- *Line M* The perpendicular distance between the roof of the IOC (being the orbital floor) and line B at its midpoint (blue line).
- *Line H* Highest distance from line B to the roof of the IOC (being the orbital floor) (orange line).
- *Distance m* The distance from the midpoint of line B to S (light blue).
- *Distance h* The distance from line H to the IOF (light orange).

Angles between the IOC and specific landmarks were evaluated to determine the direction of the IOC in relation to adjacent anatomical structures (Figs. 3, 4).

- *Anterior angle (A-ant)* (Fig. 3) The angle between the anterior part of the IOC (green line) and the axial plane being parallel to the nasal floor/the hard palate (white line).

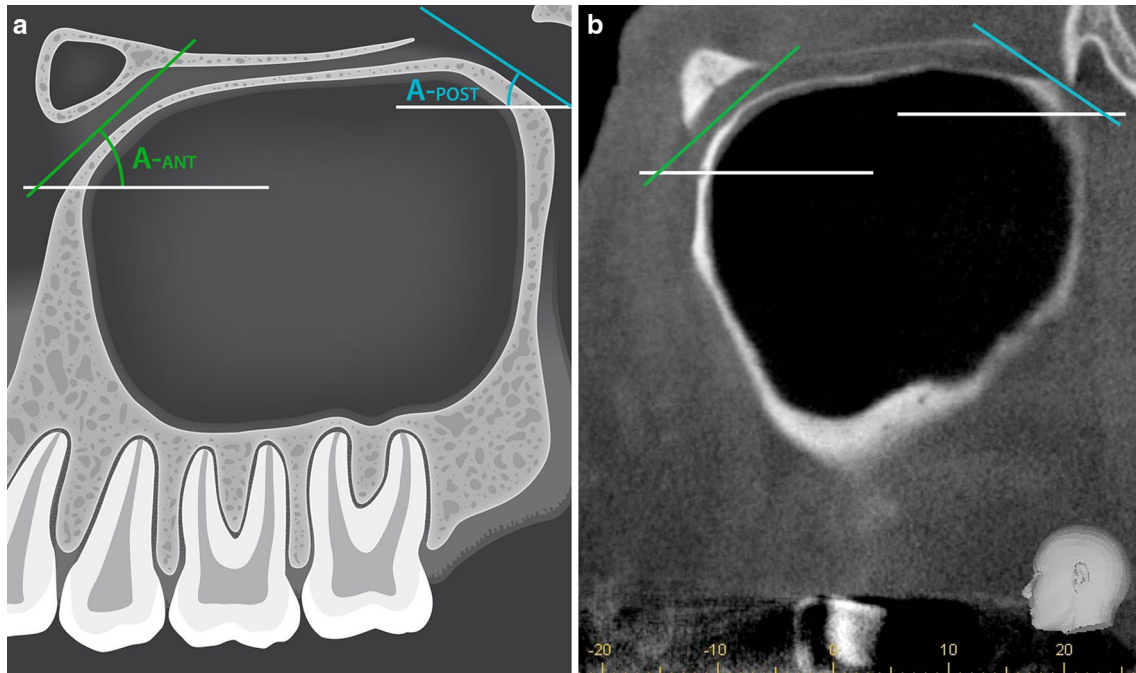


Fig. 3 The schematic illustration (a) and a representative CBCT image (b) show the angles measured between the IOC/G and the nasal floor/hard palate in sagittal CBCT planes. The white lines are reference lines parallel to the nasal floor/hard palate in reformatted

sections: the anterior angle A-ant (green line) represents the angle between the IOC and the nasal floor; the posterior angle A-post (blue line) the angle between the IOG and the nasal floor. (Colour figure online)

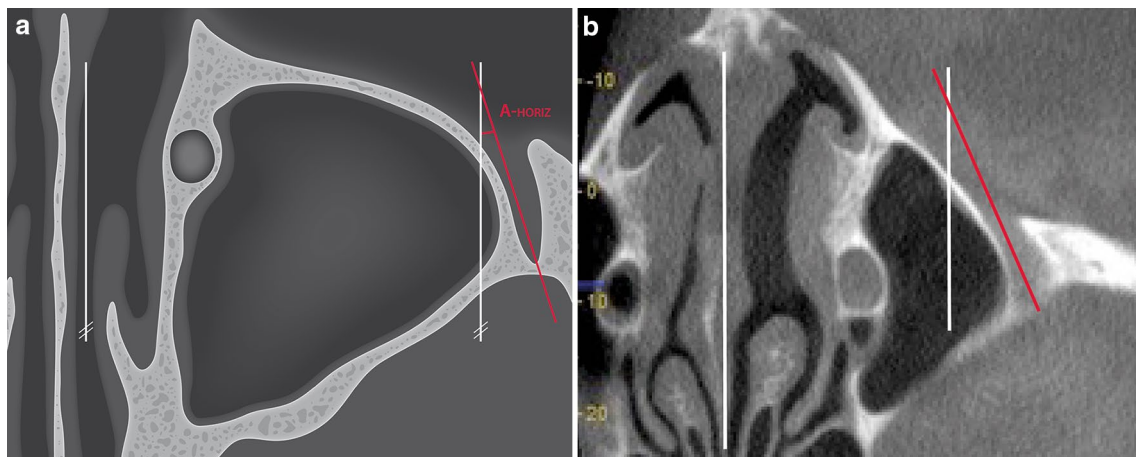


Fig. 4 A schematic illustration (a) and a representative CBCT image (b) depicting the horizontal angle A-horiz (red line) between the anterior part of the IOC and the sagittal plane being parallel to the nasal septum (white lines). (Colour figure online)

- *Posterior angle (A-post)* (Fig. 3) The angle between the IOG (blue line) and the axial plane being parallel to the nasal floor/the hard palate (white line).
- *Horizontal angle (A-horiz)* (Fig. 4) The angle between the anterior part of the IOC (red line) and the sagittal plane being parallel to the nasal septum (white line).

To classify the course of the IOC related to the maxillary sinus, a similar classification as proposed by Ference et al. [4] was applied. The categorization into three types is based on the amount of canal protrusion into the sinus. For this evaluation, the IOC morphology was analyzed using coronal CBCT planes at the level where the IOC could be best determined (Fig. 5):

- *Type 1* The IOC is totally embedded in the maxillary bone of the orbital floor or is bulging less than half of its diameter into the maxillary sinus.
- *Type 2* The IOC is located below the roof of the maxillary sinus and is partially protruding (more than half) into the maxillary sinus.
- *Type 3* The IOC is entirely protruding into the maxillary sinus.

Furthermore, the presence or absence of maxillary septa related to the IOC was analyzed (yes/no). Finally, the site where the canalis sinuosus (CSIN) branched off from the IOC was determined by dividing the IOC into three sections (Fig. 6):

- $CSIN_{IOF}$ Branching of the CSIN within the IOF.
- $CSIN_{ant}$ Branching of the CSIN within the anterior third of the IOC.
- $CSIN_{mid}$ Branching of the CSIN within the middle third of the IOC.

Statistical analysis

All data were first analyzed using descriptive statistics. Age was divided by a median split yielding two age groups for further statistical analysis. The effects of the binary independent variables (gender, side and age) on the linear measurements and angular measurements were separately evaluated with a two-sample *t* test. The effects of binary independent variables (gender, side and age) on IOC morphology type were evaluated with Pearson's Chi-squared test. Intra-observer repeatability for the linear measurements and angular measurements were assessed using interclass

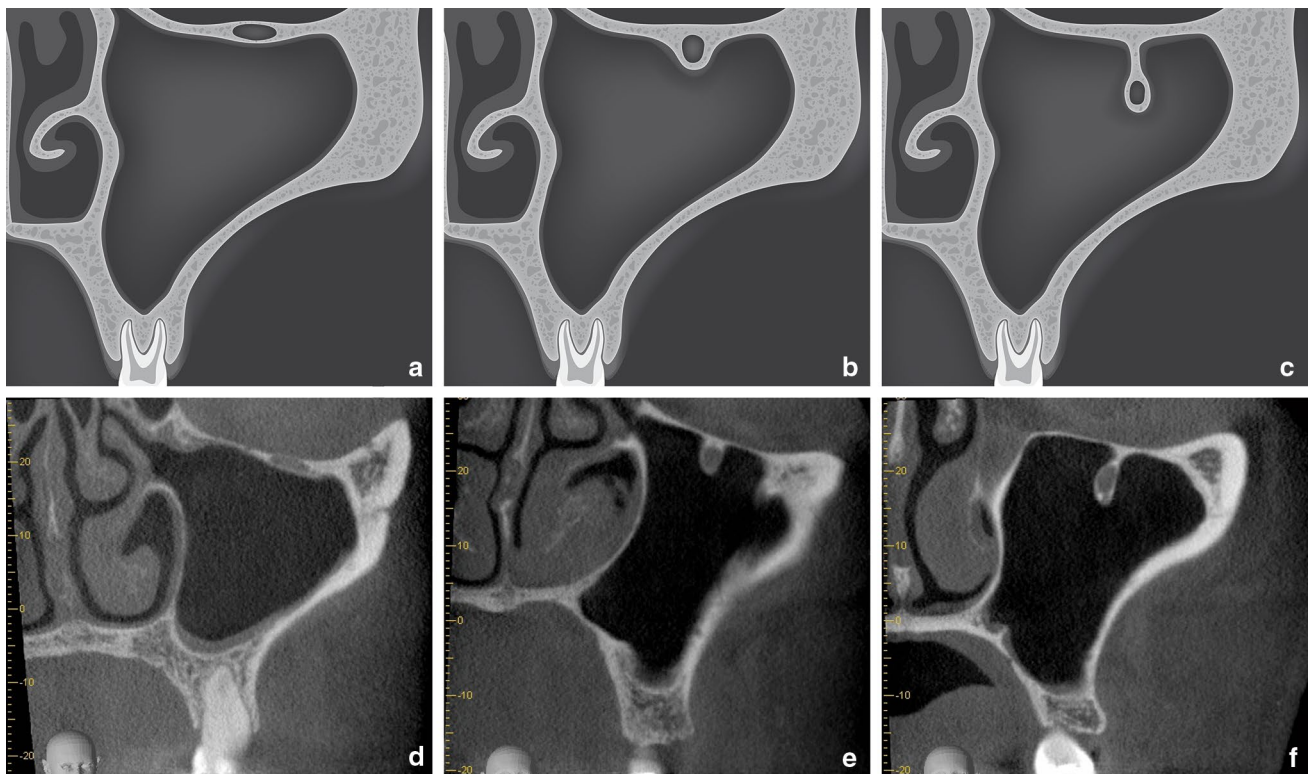


Fig. 5 Classification of IOC morphology related to the maxillary sinus depicted in a coronal plane in illustrations (a–c) and representative CBCT images (d–f). Type 1 (a, d) shows the IOC totally embed-

ded in the maxillary sinus roof; type 2 (b, e) depicts the IOC partially protruding into the maxillary sinus; type 3 (c, f) shows the IOC entirely protruding into the maxillary sinus

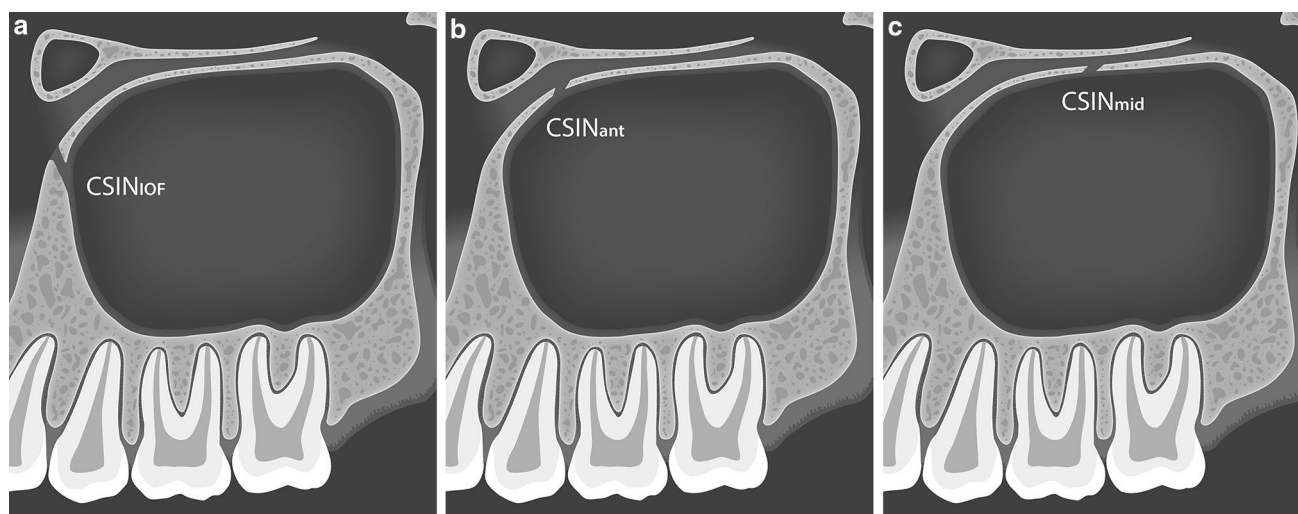


Fig. 6 The site of the canalis sinus (CSIN) branching off from the IOC was determined by dividing the IOC into three sections: the region of the IOF (CSIN_{IOF}, **a**), the anterior third of the IOC (CSIN_{ant}, **b**), the middle third of the IOC (CSIN_{mid}, **c**)

correlation (ICC) coefficients (single-rating, absolute-agreement, 2-way mixed-effect model) from duplicate measurements of 22 randomly selected samples.

The significance level chosen for all statistical tests was $p \leq 0.05$. Statistical procedures were carried out in SPSS (version 24.0, IBM, NY, USA).

Results

This study initially evaluated 976 CBCT scans of 914 patients taken during the time period from January until May 2014. In total 100 patients, 49 females and 51 males, with 127 IOCs met the inclusion criteria. The age of the patients ranged from 19 to 89 years with a mean of 58 years (median of 61 years). Out of the total of 127 IOCs evaluated, 68 were located on the right and 59 on the left side. In 27 CBCT scans, IOCs were captured bilaterally.

Intra-observer reliability of the data from the 22 randomly selected samples exhibited good to excellent agreement for the linear measurements with ICC coefficient values ranging from 0.66 to 0.98, and ICC coefficient values ranging from 0.89 to 0.98 for the angular measurements. For all linear measurements, there was a mean deviation between the two readings of 0.1 mm (range – 1.3 to 7.8 mm), and for the angular measurements of 0.1° (range – 5.0° to 10.5°).

The descriptive data of the linear measurements (mm) and angles of the IOC are summarized in Table 1. The mean total length of the IOC/G (IOF-C-S) was 29.0 mm. This value is composed of the mean distances of the IOF-C (24.4 mm) and the C-S (4.6 mm). The mean diameter of the IOC at the IOF (D_{IOF}) was 3.0 mm and 1.9 mm at the posterior margin (D_C). The mean direct distance between

IOF and S (line B) was 27.4 mm. The mean perpendicular distance (line M) at the midpoint of line B measured 5.2 mm, and the mean length of the highest perpendicular distance (line H) was 5.9 mm. The line H was generally located more anteriorly and closer to the IOF than line M at the midpoint (mean distance to IOF $h = 6.6$ mm, $m = 13.7$ mm, respectively). The mean angle A-ant measured 48.9°, the mean A-post was 12.0°, and the mean A-horiz 20.3° (Table 1).

With regard to the gender of the patients, the lengths of the IOF-C ($p = 0.003$), IOF-C-S ($p = 0.001$), the diameter D_{IOF} ($p = 0.020$), the line B ($p = 0.002$), the line H ($p = 0.012$), and line m ($p = 0.002$) were significantly greater in males than in females (Table 2). There were no significant differences when comparing the data between the right and left sides. The age group older than 61 years (median split) showed significantly higher values for the measurements of the diameter D_{IOF} ($p = 0.034$), the diameter D_C ($p = 0.003$), the line B ($p = 0.029$), and the line m ($p = 0.028$). The angles A-ant and A-horiz showed no significant differences with regard to gender, age or side of the face (Table 3). For A-post, male patients exhibited significantly larger values than females ($p = 0.014$).

With regard to the course of the IOC in relation to the maxillary sinus, Type 1 IOC was the most frequently diagnosed ($n = 87$, 68.5%; Table 4). No significant differences for the IOC types were seen with regard to gender, age or side. A septum in the maxillary sinus related to the IOC was present in 20 sites (15.7%). The branching site of the CSIN from the IOC could be detected in all observed IOCs ($n = 127$). The majority of the CSINs were branching off within the anterior third of the IOC (CSIN_{ant}; $n = 80$, 63.0%). In 26.8% of the cases, the CSIN branched within the IOF

Table 1 Descriptive data of the linear measurements (mm) and angles (°) performed using CBCT scans

Distances	Mean	± SD	Median	Range (min–max)
IOF-C	24.4	± 2.9	24.5	(16.9–32.8)
C-S	4.6	± 1.7	4.5	(0.3–10.9)
IOF-C-S	29	± 3.0	28.7	(22.1–36.5)
D_{IOF}	3.0	± 0.6	3.1	(1.8–4.4)
D_{C}	1.9	± 0.5	1.9	(0.7–3.2)
B	27.4	± 2.9	27.3	(21.4–34.7)
h	6.6	± 2.7	6.1	(2.1–15.8)
H	5.9	± 1.0	5.9	(3.7–9.5)
m	13.7	± 1.4	13.7	(10.8–17.4)
M	5.2	± 1.0	5.2	(2.1–8.3)
Angle	Mean	± SD	Median	Range (min–max)
A-ant	48.9	± 7.5	49.5	(26.0–64.9)
A-post	12.0	± 7.7	10.5	(0.6–42.8)
A-horiz	20.3	± 7.9	19.3	(4.1–44.0)

Abbreviations of the linear measurements: *IOF-C* length of the infraorbital canal IOC, *C-S* length of the infraorbital groove IOG, *IOF-C-S* IOF/G complex, D_{IOF} diameter of the IOC at the IOF, D_{C} diameter of the IOC at the posterior margin, *B* direct distance between IOF and S, *H* highest perpendicular distance to B, *h* distance from H to the IOF, *M* perpendicular distance at the midpoint of B, *m* distance from M to S

Abbreviations of the angular measurements: *A-ant* anterior angle, *A-post* posterior angle, *A-horiz* horizontal angle

(CSIN_{IOF} ; $n = 34$), and in 10.2% within the middle third of the IOC (CSIN_{mid} ; $n = 13$).

Discussion

This study evaluated the dimensions, morphology and anatomical relations to adjacent structures of the IOC/G by means of CBCT scans. To the best of our knowledge, only Orhan et al. [12] have published a study analyzing the morphology of the IOC/G using CBCT imaging. CBCT has an important role in the diagnosis and treatment planning of craniofacial disorders [12]. This imaging technique is routinely used for presurgical evaluation in medical disciplines such as oto-rhino-laryngology or maxillofacial surgery [12]. It is an adequate imaging method to evaluate the paranasal sinuses and contiguous structures [16], and it has been recommended as a dose-sparing technique, compared to standard medical CT scans [10].

Zygomaticomaxillary bone fractures such as blow-out fractures can cause trauma to the ION by compression of the nerve, which may result in permanent paresthesia [6, 11]. The management of these fractures as well as other types of operations such as tumor surgeries, Caldwell-Luc procedures, and Le-fort-type osteotomies can also result in iatrogenic damage to the ION [6]. During these interventions and also due to trauma, the infraorbital nerve is stretched and exposed by orbital floor displacement, and thus is at a great risk for injury [8]. Furthermore, to perform an infraorbital nerve block, the surgeon must be aware of the IOC's

angulation and length to avoid damage to orbital structures [9, 12]. Therefore, detailed knowledge of the anatomy and location of the IOC within the facial bony structures is beneficial and should be mandatory to guarantee safe surgical and anesthetic procedures.

In this study, the mean length of the IOC/G (IOF-C-S) was 29 mm—comprising the IOC with 24.4 mm and the IOG with a mean value of 4.6 mm. Przygocka et al. [13] reported similar measurements for the IOC/G in 35 human dry skulls: 27.7 mm on the right side and 28.1 mm on the left side, respectively. Although the present study used the same definition of the IOC and the IOG, Przygocka's results exhibited a shorter IOC (14.2 mm on the right and 13.7 mm on the left side) but a longer IOG (13.5 mm on the right and 14.1 mm on left side) compared to the data in the present study. Kazakayasi et al. [6] analyzed 35 adult skulls using cephalometric (2-dimensional) analysis. They reported on average an IOC length of 23 mm and an IOG length of 6 mm. Hwang and co-workers [5] used a three-dimensional reconstruction of segmented CT scans to perform measurements. In their analysis, the length of the IOC was 11.7 mm and the IOG was 16.7 mm. These marked differences compared to the values of the present study may be explained by Hwang's definition of these anatomic entities: "The IOC and IOG were discriminated by the change in direction, where the upward and lateral course of the IOC was changed to be parallel to the orbital floor, instead of the coverage of the orbital floor bone" [5]. This definition was also used by Orhan and co-workers [12] in their analysis of the IOC using CBCT. The canal was defined as the distance from the

Table 2 Influence of gender, age, and side on the linear measurements (mm) of the IOF/C/G evaluated on CBCT scans

Measurements (mm)	Length IOF-C		Length C-S		Length IOF-C-S		D _{IOF}		D _C		B		H		h		M		m	
	Mean	±SD	Mean	±SD	Mean	±SD	Mean	±SD	Mean	±SD	Mean	±SD	Mean	±SD	Mean	±SD	Mean	±SD	Mean	±SD
Male (n = 62)	25.2	3	4.7	1.9	29.9	3.2	3.2	0.6	2	0.6	28.2	3.1	6.1	1.2	6.6	2.9	5.3	1.2	14.1	1.6
Female (n = 65)	23.7	2.6	4.5	1.6	28.2	2.5	2.9	0.6	1.8	0.4	26.6	2.4	5.7	0.8	6.5	2.5	5.1	0.9	13.3	1.2
<i>p</i> value of two-sample <i>t</i> test	0.003		0.529		0.001		0.020		0.091		0.002		0.012		0.795		0.183		0.002	
Right (n = 68)	24.3	2.9	4.5	1.8	28.9	2.9	3	0.6	1.9	0.4	27.2	2.7	5.9	1.1	6.5	2.8	5.2	1	13.6	1.3
Left (n = 59)	24.6	2.9	4.7	1.6	29.3	3.1	3.1	0.6	1.8	0.5	27.6	3.1	5.9	1	6.7	2.6	5.2	1.1	13.8	1.5
<i>p</i> value of two-sample <i>t</i> test	0.571		0.71		0.445		0.302		0.223		0.496		0.954		0.698		0.828		0.574	
Age ≤ 61 (n = 64)*	24.1	2.5	4.5	1.8	28.6	2.7	2.9	0.6	1.8	0.4	26.8	2.5	5.8	1	6.3	2.3	5.2	1	13.4	1.3
Age > 61 (n = 63)	24.8	3.3	4.7	1.7	29.5	3.2	3.2	0.6	2	0.5	27.9	3.1	5.9	1.1	6.9	3.1	5.2	1.1	14	1.6
<i>p</i> value of two-sample <i>t</i> test	0.16		0.437		0.069		0.034		0.003		0.029		0.663		0.224		0.78		0.028	
Total (n = 127)	24.4	2.9	4.6	1.8	29	3	3	0.6	1.9	0.5	27.4	2.9	5.9	1	6.6	2.7	5.2	1	13.7	1.4

Bold = statistically significant (*p* < 0.05)

Abbreviations of the linear measurements: IOF-C length of the infraorbital canal IOC, C-S length of the infraorbital groove IOG, IOF-C-S IOF/G complex, D_{IOF} diameter of the IOC at the IOF, D_C diameter of the IOC at the posterior margin, B direct distance between IOF and S, H highest perpendicular distance to B, h distance from H to the IOF, M perpendicular distance at the mid-point of B, m distance from M to S

*Age grouped by a median split

Table 3 Influence of gender, age, and side of the IOC angles (°) measured on CBCT scans

Angles (°)	A-ant		A-post		A-horiz	
	Mean	±SD	Mean	±SD	Mean	±SD
Male (<i>n</i> = 62)	48.3	±7.4	13.7	±9.0	19.3	±6.7
Female (<i>n</i> = 65)	49.5	±7.7	10.3	±6.0	21.2	±8.8
<i>p</i> value of two-sample <i>t</i> test	0.377		0.014		0.161	
Right (<i>n</i> = 68)	49.0	±8.3	11.4	±7.8	19.8	±7.6
Left (<i>n</i> = 59)	48.8	±6.6	12.6	±7.7	20.8	±8.2
<i>p</i> value of two-sample <i>t</i> test	0.910		0.393		0.445	
Age ≤ 61 (<i>n</i> = 64)	49.7	±7.1	12.6	±7.8	19.8	±8.4
Age > 61 (<i>n</i> = 63)	48.1	±7.9	11.4	±7.7	20.8	±7.3
<i>p</i> value of two-sample <i>t</i> test	0.248		0.381		0.480	
Total (<i>n</i> = 127)	48.9	±7.5	12	±7.7	20.3	±7.9

Bold = statistically significant ($p < 0.05$)

Abbreviations of the angular measurements: *A-ant* anterior angle, *A-post* posterior angle, *A-horiz* horizontal angle

Table 4 Distribution and frequency of the IOC morphology with regard to gender, age, and side

Morphology	Type 1		Type 2		Type 3		<i>p</i> value*
	<i>n</i>	%	<i>n</i>	%	<i>n</i>	%	
Male (<i>n</i> = 62)	44	71.0	11	17.7	7	11.3	0.159
Female (<i>n</i> = 65)	43	66.2	19	29.2	3	4.6	
Right (<i>n</i> = 68)	45	66.2	17	25.0	6	8.8	0.818
Left (<i>n</i> = 59)	42	71.2	13	22.0	4	6.8	
Age ≤ 61 (<i>n</i> = 64)	41	64.1	17	26.6	6	9.4	0.545
Age > 61 (<i>n</i> = 63)	46	73.0	13	20.6	4	6.3	
Total (<i>n</i> = 127)	87	68.5	30	23.6	10	7.9	

Statistically significant ($p < 0.05$)

Definitions of the type of IOC morphology: *Type 1* IOC totally embedded in the maxillary sinus roof, *Type 2* IOC partially protruding into the maxillary sinus, *Type 3* IOC entirely protruding into the maxillary sinus

*Chi-squared test

center of the IOF to the portion where the axis of the IOC changed. In contrast, the length of the IOG was defined as the sum of the IOG not covered by bone and the portion that was parallel to the orbital floor but covered by bone. However, their findings for the IOC length were longer than in the present study (28.3 mm on the right and 27.5 mm on left side), whereas the values for the IOG were similar (3.5 mm on the right and the left side).

Comparing the measurements of the male and female patients, significantly greater values could be found in males for IOC, IOC/G, D_{IOF} , B and H (Table 2). Orhan et al. [12] have shown significantly larger measurements for the IOC and IOG in male patients as well. These findings were corroborated by Hwang et al. [5] who found the length of the IOG in males to be significantly larger.

Looking at differences related to the right and the left side of the measured sites, there were no significant differences in the linear measurements found in the present study. With regard to the age, patients older than 61 years showed

significantly larger measurements for the D_{IOF} , the D_C , the distance B, and the distance m. In contrast, Orhan et al. [12] did not find a significant difference comparing the lengths of the IOC and the IOG in three age groups.

To perform an ION block, the surgeon must insert the needle upward and laterally and advance it within the IOC [9]. Advancement into the IOG has been reported to potentially result in damage of the orbital structures [5]. Nevertheless, with accurate knowledge of the direction of the IOC, the surgeon can establish a good angle of the needle entry and easily advance the needle into the IOC. Hwang et al. [5] used a three-dimensional reconstruction after segmentation of CT scans and identified anatomic landmarks and planes associated with the IOF. The measurements respective angles were performed on these three-dimensional models [5]. In this study, a similar approach was used to assess angle measurements. To identify the axis of the IOC, vertical and horizontal reference planes were determined. The angle A-ant, between IOC and the horizontal plane

being parallel to the nasal floor, was 48.9° . This was a very similar value compared to Hwang's result for the same type of measurement (46.7°). The angle A-horiz, between IOC and the vertical plane being parallel to the nasal septum, was 20.3° . Hwang et al. measured a smaller angle of 13.2° . In the present study, the angles A-ant and A-horiz showed no significant differences with regard to gender, age or side of the face. In contrast, Hwang and co-workers reported a significantly greater angle of the IOC axis in relation to the horizontal plane in females [5].

The awareness of the exact IOC location and relation to the maxillary sinus is important for surgery of the maxillary sinus, indicated for the management of chronic inflammatory diseases, resection of neoplasms, or repair of the orbital floor [2]. All these procedures may cause nerve injury [3, 7, 16]. Such nerve injuries may be prevented or anticipated when identifying a descended IOC, thus instrumentation along the roof of the sinus can be planned [4].

Ference et al [4], stated in a study using CT imaging, that the protrusion of the ION within the maxillary sinus (Type 3) is a common anatomic variant seen in 12.5% of the cases. The authors note as well that the foramen of Type 3 canals is on average 2.9 mm inferiorly located compared to Types 1 and 2 canals. Furthermore, descended canals are located on average 8.6 mm below the maxillary sinus roof within the sinus [4]. In the present study, only 7.9% of the canals showed a descending variation of the IOC into the sinus lumen (Type 3), 23.6% of the IOCs were partly protruding into the sinus (Type 2), and the largest group of 68.5% showed an IOC embedded in the maxillary floor (Type 1). Yenigun et al. [19] classified three types of IOCs and their frequencies in *axial* CT accordingly: IOC protruding into the maxillary sinus with 12.3% (Type1); IOC at the floor of the maxillary sinus or partially protruding into the sinus with 51.2% (Type 2) being the most common and IOC totally embedded in the maxillary bone with 36.4% (Type 3). Since the classification in the present study was based on coronal CBCT planes, a direct comparison of the frequencies of IOC types according to Yenigun's study [19] is not possible.

Regarding gender, side or age, significant differences could not be found for a specific IOC type in the present study. These findings were corroborated by Ference et al. [4].

Regarding the findings of the present study, some limitations have to be taken into consideration. It is noted that our study population comprises a limited sample size with 127 IOCs in 100 patients. Therefore, the correlation of age and the linear/angular measurements was evaluated using two age groups divided by median split (61 years) only. These results have certainly to be interpreted with some caution, especially when comparing them to multiple age groups. Furthermore, the choice of the reproducible positions of the planes and reference landmarks has its limitations due to

the relatively small field of views of the CBCTs compared to CT scans. On CTs, the sella turcica or the nasion can be used as stable reference structures [20]. A further limitation of this study was that the measurements were performed by one observer only.

Conclusions

Prevention of infraorbital nerve injuries and complications during surgery or anesthesia may be accomplished by identifying the characteristics and variants of the IOC/G. These include the length of the IOC/G complex, the angulations of the IOC axis relative to the axial (A-ant) and the sagittal planes (A-horiz), and the IOC morphology (Type 1–3). The presented data contributes to the knowledge of the IOC/G anatomy for preoperative treatment planning by means of CBCT imaging, which may help to estimate the risk of ION trauma during surgical interventions.

Acknowledgements The authors thank Bernadette Rawyler, Medical Illustrator, School of Dental Medicine, University of Bern, Switzerland for the schematic illustrations. The authors are also grateful to Ms. Kar Yan Li, Centralised Research Lab, Faculty of Dentistry, The University of Hong Kong, for her valuable assistance regarding the statistical analysis.

Author contributions M Fontollet: Protocol/project development, data collection, data analysis, manuscript writing. MM Bornstein: Protocol/project development, data analysis, manuscript editing. Th von Arx: Protocol/project development, manuscript editing.

Funding No grants or funding have been received for this study.

Compliance with ethical standards

Conflict of interest The author(s) declare that they have no conflict of interest.

References

1. Caspersen LM, Christensen IJ, Kjaer I (2009) Inclination of the infraorbital canal studied on dry skulls expresses the maxillary growth pattern: a new contribution to the understanding of change in inclination of ectopic canines during puberty. *Acta Odontol Scand* 67:341–345
2. Chandra RK, Kennedy DW (2004) Surgical implications of an unusual anomaly of the infraorbital nerve. *Ear Nose Throat J* 83:766–767
3. Cutler JL, Duncavage JA, Matheny K, Cross JL, Miman MC, Oh CK (2003) Results of Caldwell-Luc after failed endoscopic middle meatus antrostomy in patients with chronic sinusitis. *Laryngoscope* 113:2148–2150
4. Ference EH, Smith SS, Conley DC, Chandra RK (2015) Surgical anatomy and variations of the infraorbital nerve. *Laryngoscope* 125:1296–1300
5. Hwang SH, Kim SW, Park CS, Kim SW, Cho JH, Kang JM (2013) Morphometric analysis of the infraorbital groove, canal,

- and foramen on three-dimensional reconstruction of computed tomography scans. *Surg Radiol Anat* 35:565–571
6. Kazakayasi M, Ergin A, Ersoy M, Bengi O, Tekdemir I, Elhan A (2001) Certain anatomical relations and the precise morphometry of the infraorbital foramen-canal and groove: an anatomical and cephalometric study. *Laryngoscope* 111:609–614
 7. Kim E, Duncavage JA (2010) Prevention and management of complications in maxillary sinus surgery. *Otolaryngol Clin North Am* 43:865–873
 8. Lawrence JE, Poole MD (1992) Mid-facial sensation following craniofacial surgery. *Br J Plast Surg* 45:519–522
 9. Lee UY, Nam SH, Han SH, Choi KN, Kim TJ (2006) Morphological characteristics of the infraorbital foramen and infraorbital canal using three-dimensional models. *Surg Radiol Anat* 28:115–120
 10. Ludow JB, Ivanovic M (2008) Comparative dosimetry of dental CBCT devices and 64-slice CT for oral and maxillofacial radiology. *Oral Surg Oral Med Oral Pathol Oral Radiol Endod* 106:106–114
 11. Olenczak JB, Hui-Chou HG, Aguila DJ III, Shaeffer CA, Dellon AL, Manson P (2015) Posttraumatic midface pain: clinical significance of the anterior superior alveolar nerve and canalis sinuosus. *Ann Plast Surg* 75:543–547
 12. Orhan K, Misirli M, Aksoy S, Seki U, Hincal E, Ormeci T, Arslan A (2016) Morphometric analysis of the infraorbital foramen, canal and groove using cone beam CT: considerations for creating artificial organs. *Int J Artif Organs* 39:28–36
 13. Przygocka A, Szymański J, Jakubczyk E, Jędrzejewski K, Topol M, Polgaj M (2013) Variations in the topography of the infraorbital canal/groove complex: a proposal for classification and its potential usefulness in orbital floor surgery. *Folia Morphol* 72:311–317
 14. Scarfe WC, Langlais RP, Ohba T, Kawamata A, Maselle I (1995) Panoramic radiographic patterns of the infraorbital canal and anterior superior dental plexus. *Dentomaxillofac Radiol* 27:85–92
 15. Song WC, Kim JN, Yoo JY, Lee JY, Won SY, Hu KS, Kim HJ, Koh KS (2012) Microanatomy of the infraorbital canal and its connecting canals in the maxilla using 3-D reconstruction of microcomputed tomographic images. *J Craniofac Surg* 23:1184–1187
 16. Tewfik MA, Wormald P-J (2013) Chapter 9: complications in endoscopic sinus surgery. In: Bernal-Sprekelsen M, Carrau RL, Dazert S et al (eds) *Complications in otolaryngology-head and neck surgery*. Thieme, New York
 17. Von Arx T, Lozanoff S, Sendi P, Bornstein MM (2013) Assessment of bone channels other than the nasopalatine canal in the anterior maxilla using limited cone beam computed tomography. *Surg Radiol Anat* 35:783–790
 18. Wanzeler AMV, Marinho CG, Melo Alves S Jr, Manzi FR, Mesquita Tuji F (2013) Anatomical study of the canalis sinuosus in 100 cone beam computed tomography examinations. *Oral Maxillofac Surg* 19:49–53
 19. Yenigun A, Gun C, Uysal II, Nayman A (2016) Radiological classification of the infraorbital canal and correlation with variants of neighboring structures. *Eur Arch Otorhinolaryngol* 273:139–144
 20. Zhao ZM, Zhu Y, Huo R, Su JR, Gao F (2014) Three-dimensional cephalometric analysis of adolescents with cleft lip and palate using computed tomography-guided imaging. *J Craniofac Surg* 25(6):1939–1942